University of Glasgow

Triantafyllou, C., Pagan, D. C. and McBride, A. (2022) Quantifying the effect of macrozones on the cold-dwell fatigue response of UD-Rolled Ti-6Al-4V using high-energy X-ray diffraction. *Materials Science and Engineering A: Structural Materials Properties Microstructure and Processing*, 834, 142498.

(doi: 10.1016/j.msea.2021.142498)

This is the Author Accepted Manuscript.

There may be differences between this version and the published version. You are advised to consult the publisher's version if you wish to cite from it.

https://eprints.gla.ac.uk/260362/

Deposited on: 10 December 2021

Enlighten – Research publications by members of the University of Glasgow
http://eprints.gla.ac.uk

Quantifying the Effect of Macrozones on the Cold-Dwell Fatigue Response of UD-Rolled Ti-6Al-4V using High-Energy X-Ray Diffraction

Christos Triantafyllou[a,*], Darren C. Pagan[b], Andrew McBride[a]

[a] *Materials & Manufacturing Research Group, James Watt School of Engineering, University of Glasgow, Glasgow, UK*

[b] *Department of Materials Science and Engineering, The Pennsylvania State University, PA, USA*

Abstract

High-energy X-ray diffraction is used to investigate the evolution of elastic lattice strains in rolled Ti-6Al-4V specimens during cyclic loading in-situ with and without the inclusion of a 120 s dwell period. A 1 mm segment of the gauge section is monitored throughout the first 100 cycles for specimens extracted along the rolling direction (RD), the transverse direction (TD) and 45° between the two, to explore the effects of texture on the evolution of the micromechanical response. Five families of lattice planes from the hexagonal α phase are analysed with emphasis on lattice strain measured at the peak of each cycle, while macroscopic strain accumulation is simultaneously monitored via Digital Image Correlation. In cyclic loading conditions including a dwell period at load, a prominent increase in elastic strains is observed in prismatic and basal lattice planes with the specimen loaded 45° from the rolling direction. In the absence of dwell, both RD and TD specimen orientations exhibited subtle cyclic hardening in all families of lattice planes probed despite negligible evolution in accumulated macroscopic plastic strain. Estimations of lattice orientation-dependent stresses are also presented using directional moduli to examine redistribution of load across sets of grains with the increasing cycle count.

Keywords: Titanium, Fatigue, Cold-Dwell, Diffraction, Lattice Strain

1. Introduction

Since their introduction as commercial materials in the late 1940s, titanium alloys have become established as the primary material of choice for a variety of demanding applications in the aerospace sector, jet engines in particular. Titanium alloys generally exhibit very good specific strength, good corrosion resistance and, in some cases, very good fatigue strength [1]. Nonetheless, the deleterious effects of prolonged exposure to sustained and repeated, sub-yield load on different titanium

*Corresponding author.
Email address: c.triantafyllou.1@research.gla.ac.uk (Christos Triantafyllou)

alloys have been the subject of research for decades due to the complex interactions between microstructural features that drive fatigue failure. Notably, the presence of an extended dwell period at peak load (conditions encountered during the cruising phase of a flight cycle) has been shown to negatively affect many titanium alloys, producing a significant reduction in fatigue life [2–7]. Sensitivity to these loading conditions, termed cold dwell fatigue, is dependent on the complex interactions between composition, microstructure and processing history. For example, coarse microstructures of Ti-6Al-4V (Ti64) and, in particular, those treated above the β transus and then cooled slowly, have exhibited higher sensitivity to cold dwell [8]. However, fine-grained microstructures such as fully lamellar or Widmanstätten types of microstructures have shown insensitivity to the dwell phenomenon [9]. This behaviour has led to large factors of safety being used in the design of critical parts, resulting in heavier jet engine components requiring more regular inspections. A significant body of literature has emerged proposing numerous contributing factors to dwell fatigue failures. The need for in-situ experiments in which one can 'observe' the microstructural and micromechanical evolution driving the failure is motivated by the attempt to relate multiple contributing factors to the existing theory.

Macroscopically, dwell failures differentiate themselves from ordinary fatigue or creep failures as they are associated with the presence of quasi-cleavage facets which nucleate beneath the surface and not necessarily at high-stress concentration points [3]. At the grain scale, it is generally accepted that the stress redistribution between 'soft' and 'hard' grains is driving the facet formation and subsequently the premature failure. A grain is characterised as 'soft' when its crystallographic c axis is oriented relative to the loading axis in such a way that makes crystallographic slip (or simply slip) on prismatic or basal slip systems favourable. Conversely, a grain with its c axis oriented parallel or near-parallel to the loading axis is described as 'hard' as slip cannot easily occur. The dwell period allows for time-sensitive accumulation of dislocations resulting from plasticity, particularly in areas where there is low slip transmission, which subsequently increases the stress at the 'hard' grain boundary [3, 10]. It has been shown that grains with a c axis deviation of up to 15° from the loading axis can be characterised as 'hard' and constitute potential sites for facet formation on failure slip planes that lie perpendicular to the loading axis [11, 12].

Even though basal planes have been widely regarded as the prime locations for facet formation [3], Sackett et al [13] found that basal slip had not played a key role in the dwell fatigue failures of Ti685 that was heat-treated to result in abnormally large grains. Single-crystal, micro-pillar experiments and crystal plasticity modelling using Ti6242 by Zhang et al [14] showed that even though the strain-rate sensitivity of basal planes is higher than that for prisms, the difference between them is smaller than had been previously reported. High cycle fatigue (HCF) experiments by Bantounas et al [15] using Ti64 plate indicated that macrozones with their c axis close to the loading direction displayed facets at the fracture surface while those perpendicular to the loading axis were proposed to have acted as barriers to slip that displayed irregular fracture morphologies.

As lattice orientation clearly plays a critical role in the dwell fatigue process, texture and macrozones (large regions of grains with similar orientation) have a significant effect on failure initiation and propagation during cyclic loading. A comprehensive study by Le Biavant et al [16] indicated that cracks in textured Ti64 initiated on basal or prismatic planes, with a macrozone that had an orientation favourable for slip appearing heavily damaged after being fatigued. Hémery et al [17] subjected Ti64 to monotonic, sub-yield loading which revealed that slip activated earlier in microtextured regions with strong basal texture and that basal slip was found to activate before prismatic slip. Even though the orientation of the macrozone is directly linked to the crack initiation in α grains, it does not affect crack growth characteristics once the crack length exceeds the size of the macrozone [16]. A study by Zhang et al [18] supports the case for crack initiation taking place at the interface between macrozones, one of which being more and one being less favourably oriented for slip. A model by Pilchak [19] showed that in the presence of dwell, the size of the microtextured regions (MTRs) in titanium alloys has a much larger effect on fatigue life than the initial crack size.

In this context, the role of the deformation mode during raw material processing should be acknowledged as a key determinant of texture symmetry and intensity. At relatively low deformation temperatures, unidirectionally-rolling Ti64 will form a basal/transverse texture; as the rolling temperature approaches the β transus a pure transverse texture can be obtained, while processing above the transus can result in more intricate textures which could also include grains with their c axis along the Rolling Direction (RD) [1]. More specifically, in commercially rolled Ti64 products, most grains are found to preferentially orient themselves so that their c axes are perpendicular to the rolling direction [20]. However, Bantounas et al [21] noted the presence of two macrozone categories in UD-rolled Ti64; one with the grains' c axes lying perpendicular to the RD, and one with the c axes lying parallel to the RD with the former occupying a larger proportion of the scanned area. It is also worth mentioning that data by Bache & Evans [20] on UD-rolled Ti64 suggests that even though specimens cut along the transverse direction (TD) exhibited a superior modulus of elasticity, yield stress and UTS compared to specimens along the RD, this was largely offset by poor ductility.

There is currently limited direct experimental validation of the dwell fatigue failure mechanisms due to the difficulty in bridging the gap between microscale experiments, that do not necessarily represent the bulk behaviour and macroscale experiments that cannot be used to reliably tie the macroscopic response to the grain-level interactions beyond post-event examinations. Synchrotron diffraction offers the advantage of being able to examine grain-scale response through measurement of lattice strains in-situ while probing a statistically significant number of grains. In the last decade, synchrotron diffraction has been used more widely to characterise the behaviour of titanium alloys, including of forged Ti64 under tensile loading [22], mill-annealed Ti64 [23], CP Ti [24, 25], Ti-7Al [26] and equiaxed Ti64 [27, 28]. While some of the previous work pays attention to stress relaxation effects during extended hold periods in CP Ti [25], there are no studies that examine the lattice strain response of dwell fatigue over a sustained number of cycles.

In order to elucidate the aforementioned mechanisms and begin to determine the role of the processing route, the evolution of lattice strains of unidirectionally-rolled (UD) Ti64 in dwell and non-dwell cyclic loading conditions is tracked in-situ using high-energy X-ray diffraction. Due to the strong MTR presence along a single direction, the UD-rolled product was chosen to impose distinctly different conditions for slip favourability by extracting specimens along the RD, TD and 45° between the two. Further information about the material and the microtexture present is provided in Section 2, as well as a detailed overview of the experimental setup. The macroscopic strain, lattice strain and estimated lattice stress results are provided in Section 3. This is followed by a comprehensive discussion.

2. Experiments

2.1. Material

The material studied is UD-rolled Ti64 plate supplied by Rolls-Royce plc. The ingot was initially β worked then α/β worked in an open die forge to produce the intermediate slab and finally α/β rolled in one direction gradually reducing its thickness. Lastly, the material was creep flattened and machined to the finished product thickness of 10 mm. The microstructure of the as-received plate was examined using a Zeiss Sigma SEM. Two representative images are shown in Fig. 1 which reveal a bimodal microstructure typical for a hot-rolled Ti64 product. This consists of primary α phase grains which appear both as near-equiaxed with the width ranging from 5 µm to 20 µm, as well as grains with extensive elongation along the TD/RD plane, as shown in Fig. 1(b). Some of these fairly homogeneous α phase regions have been found to measure up to 110 µm, while the height of such grains does not tend to exceed 10 µm along the normal direction (ND). A smaller proportion of secondary α grains is also observed with individual α_s lamellae measuring 1-2 µm in thickness. The β phase is concentrated along grain boundaries, as well as in the form of finer laths within secondary alpha grains. An energy-dispersive X-ray spectroscopy (EDS) analysis was carried out on the same as-received specimen at a magnification of 3000x and a pixel size of 0.1 µm covering an area of 103 µm x 77 µm. The results of this analysis, along with the supplier's nominal composition of the plate product are summarised in Table 1. Finally, four SEM images were processed to estimate the area fraction of the β phase, which was found to be 5.01% on average.

Table 1: Nominal and measured composition of the UD-rolled Ti64 plate.

	Ti	**Al**	**V**	**N**	**C**	**O**	**Fe**	**H**	**Total Resid.**
Nominal	Balance	5.5-6.7	3.5-4.5	0.05	0.08	0.20	0.40	0.015	0.4
EDS Sample	Balance	6.0	4.0						

An FEI Quanta 200F was used for all EBSD scans of the raw plate material and the dwell specimens, as shown in Fig. 2(a) and 3, respectively. In the large area EBSD map, orientations are coloured relative to the transverse direction (TD) as is common for rolled products, such that red indicates a basal normal pointing along the TD. The large area scan shown in Fig. 2(a) consists of 21 tiles at 230x magnification

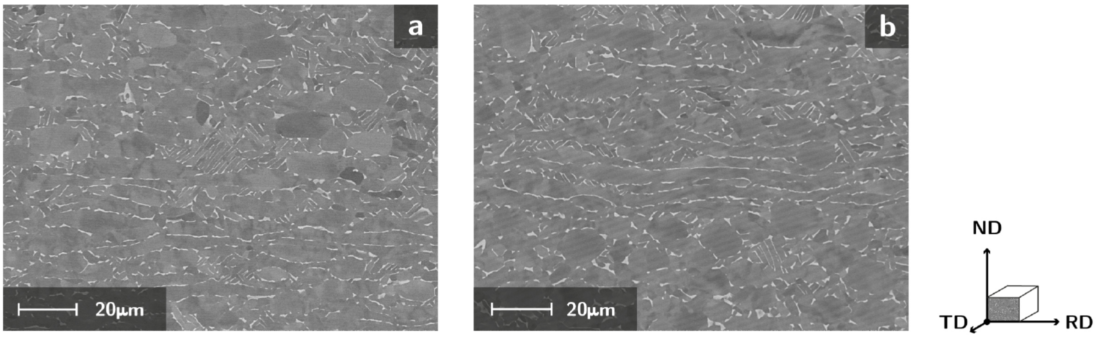

Figure 1: Angle selective Backscatter (AsB) images of the as-received material highlighting two distinct microstructural regions. (a) shows near equiaxed primary α grains (dark grey regions) with a smaller proportion of the β phase (light grey regions) concentrated along grain boundaries. Secondary α grains are also found consisting of smaller α_s lamellae and finer β. (b) shows a different region of the material where the elongation of α grains is prominent due to the effect of rolling.

and a step size of 3.5 µm. The synchrotron specimens covered an area of $<0.9\,\mathrm{mm}^2$ and a step size of 2 µm was used to scan the entire cross-sectional area at the gauge in a single scan at a magnification of 110x. Tiles were manually stitched using the OIM Analysis [29] software and subsequent processing of all the EBSD scans and visualisation was carried out using a custom MTEX routine [30]. Fig. 2(b) shows the (0001), $(10\bar{1}0)$, and $(11\bar{2}0)$ orientation pole figures to visualise the calculated orientation density function (ODF) (i.e. kernel density estimation) from the same region probed using EBSD.

The scans reveal a strong texture, primarily consisting of α grains with their crystallographic c axis along the TD and, to a much lesser extent, along the RD which is also clearly seen in the pole figures in Fig. 2(b). This is a typical texture for the UD-rolled plate [31]. The large area scan in Fig. 2(a) shows that macrozones are prevalent in the scanned area (large regions with the [0001] direction aligned with TD), and highlights the presence of macrozones with widths that extend up to approximately 1 mm to 2 mm. This is an important consideration for the specimens used as the gauge diameter does not exceed 1 mm.

Specimens were manufactured from the rolled plate using Electrical Discharge Machining (EDM) along three orientations; the RD, TD and 45° between the two. Taking the load frame capability and the X-ray beam size into account, it was determined that the specimen width at the gauge should not exceed 1 mm. Despite the low number of cycles that these specimens were subjected to, it was also deemed desirable to avoid using specimens with a rectangular or square cross-section. However, to limit the degree of machining-induced stress, wire EDM was used to cut an approximate hexadecagon cross-section resulting in a near-circular profile with a nominal area of $0.796\,\mathrm{mm}^2$. Due to their size and technical limitations, the specimens were not polished prior to being tested. Manufacturing tolerances led to deviations both in terms of the cross-sectional area and shape. This is highlighted in Fig. 3 with the nominal cross-section represented by the dashed lines overlaid upon the

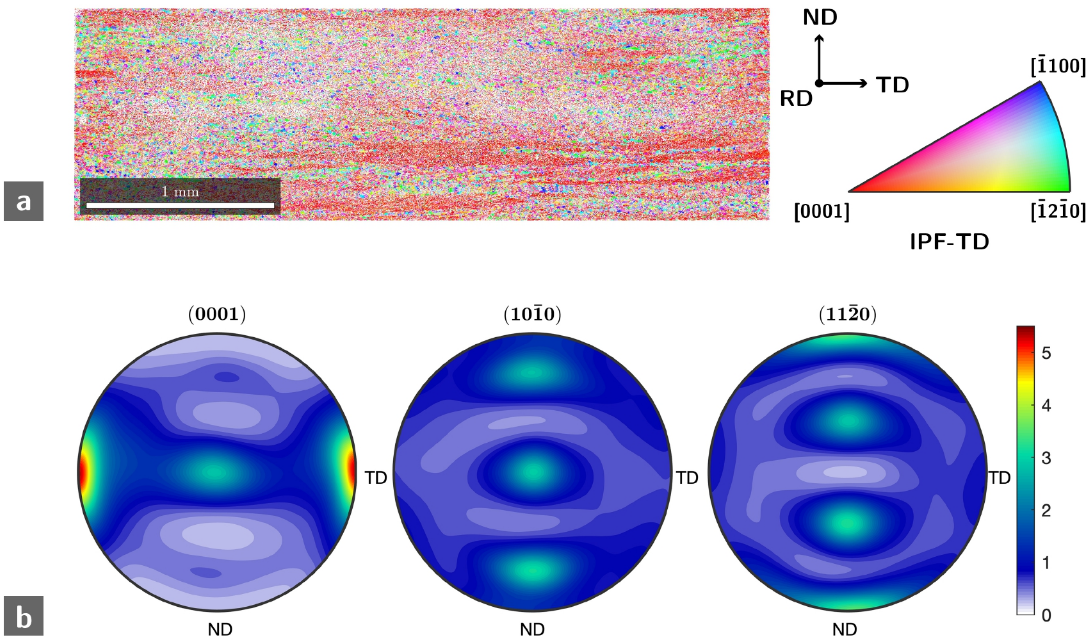

Figure 2: (a) Orientation map of a large area EBSD scan of the bulk material. Local lattice orientations are coloured with respect to the TD axis. (b) Orientation pole figures associated with the same scan (out of plane axis aligns with RD). The majority of basal normal vectors are aligned with the TD and significantly fewer fall in the band between TD and RD.

EBSD orientation maps of the true cross-sections.

Fig. 3 shows the EBSD orientation maps of the cross-sections of the specimens tested under dwell cyclic loading conditions. In Fig. 3, the orientation colouring is relative to the loading direction (LD), which is out of plane and better illustrates the strong texture differences along the loading axis. Both 45° and TD dwell specimens have a texture that is visually relatively consistent with the bulk material but have texture indices (TIs) of 2.91 and 3.62, respectively, which are both higher than the bulk TI of 2.21. While the RD specimen appears slightly more uneven, with macrozones concentrated in the top half of the cross-section examined, it has a TI of 2.79 which is closer to the bulk than the other specimens.

2.2. Experimental Method

The in-situ experiments were carried out at the F2 station of the Cornell High Energy Synchrotron Source (CHESS). A BOSE ElectroForce 3300 (3 kN) electromechanical testing frame was used to apply the load. The target stress was set to 750 MPa, approximately 85% of a representative yield stress of 880 MPa. No adjustment was applied to account for inherent differences in the orientation-specific yield stress or the small manufacturing error which resulted in slightly higher than nominal cross-sectional areas. Trapezoidal loading waves were used for both load-controlled, non-dwell and dwell experiments, using 1 s loading and unloading steps. A 0.2 s hold was added at the peak load for non-dwell experiments to capture the peak strain during each cycle. The dwell period was 120 s and both sets of experiments were terminated after 100 cycles.

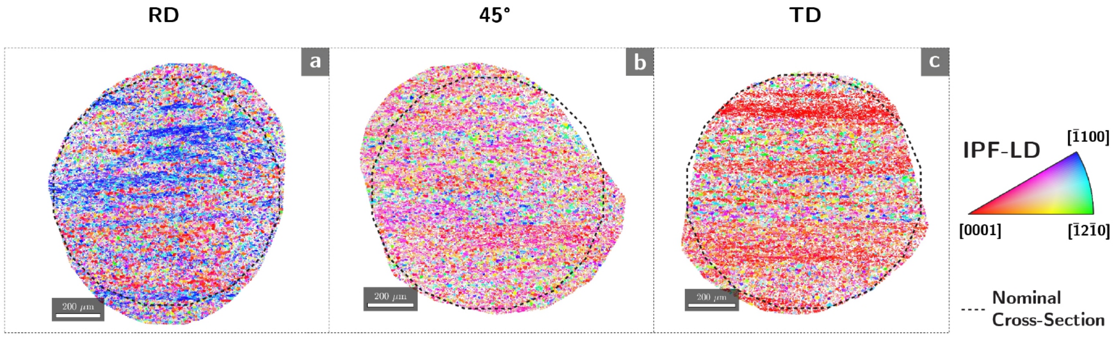

Figure 3: Electron backscatter diffraction images of the cross-sections of the dwell synchrotron specimens. The out of plane axis (LD) coincides with the loading axis. (a) The RD specimen exhibits stronger texture and MTR incidence in the top half with primarily prismatic planes being parallel to the cross-section. (b) Shows the 45° specimen and more uniform distribution of the strong textured regions that are most favourably oriented for basal slip. (c) The TD specimen also displays a macrozone distribution consistent with bulk, with a large proportion of the cross-section being taken up by basal planes being parallel to it in well-defined MTRs.

Two Dexela 2923 flat panel detectors capable of capturing images at a frequency up to 16 Hz and with a 74.8 µm pixel pitch, were used. The energy of the X-ray beam used was 61.332 keV and the effective beam size was 1 mm x 1 mm. The sample to detector distance was 795 mm and each detector panel covered an area of 3888 x 3072 pixels. Calibration was carried out using a CeO_2 standard and the beam attenuation was adjusted for each specimen. The acquisition rate for the non-dwell experiments was set to 10 Hz and for the dwell experiments to 1 Hz, which resulted in 2200 frames for the former and 12200 frames for the latter. Images of the specimens for the purposes of carrying out DIC were also captured at the same respective frequencies. DIC images were processed using GOM Correlate [32] to obtain macroscopic strain data. The experimental setup can be seen schematically in Fig. 4, including the 15° azimuthal region along the loading axis (bin).

2.3. Diffraction Data Processing

Post-processing the diffraction images was done using custom Python scripts utilising the HEXRD software package [33]. The data was processed for each detector panel separately as the area captured does not overlap, as shown in Fig. 4. Diffraction occurs when Bragg's law is satisfied; the crystallographic plane (lattice) spacing d, beam wavelength λ and diffraction angle θ are related such that:

$$\lambda = 2d \sin\theta. \tag{1}$$

For the analysis, peaks from families of lattice planes with diffraction angles 2θ less than 8° were used. Table 2 provides the diffraction angles for the α and β diffraction peaks.

Obtaining the peak positions used for elastic lattice strain determination throughout the experiment is performed by first mapping azimuthal regions of intensity on the detector to a polar coordinate system where the radial coordinate is 2θ and the

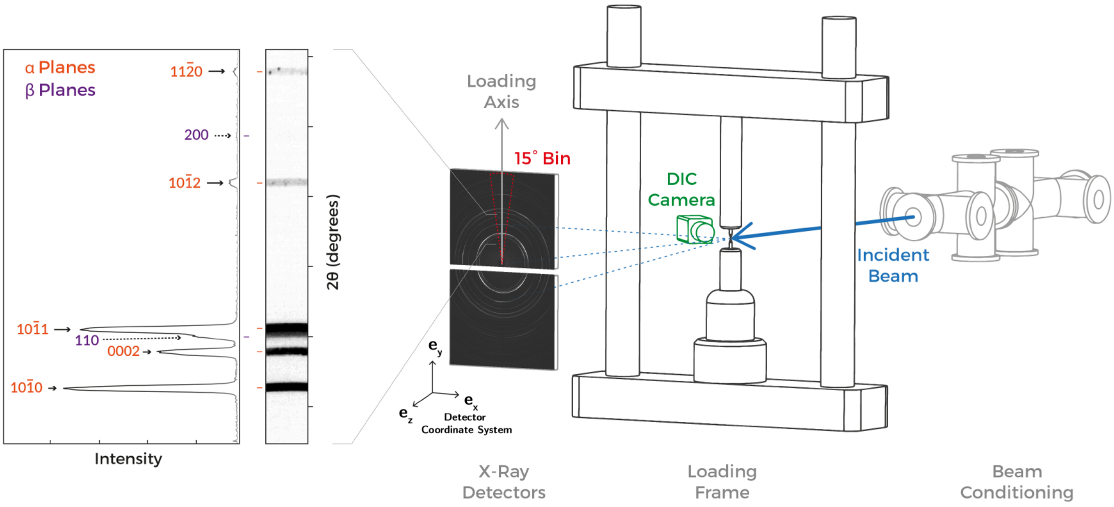

Figure 4: Simplified schematic of the experimental setup including an overview of all considered diffraction rings.

Table 2: 2θ values and their respective *hkl*s.

hkl	$\{10\bar{1}0\}$	$\{0002\}$	$\{110\}$	$\{01\bar{1}1\}$	$\{01\bar{1}2\}$	$\{020\}$	$\{11\bar{2}0\}$
Phase	α	α	β	α	α	β	α
$\boldsymbol{2\theta}$	4.59	4.96	5.14	5.21	6.76	7.27	7.95

angular coordinate is denoted η. Next, the intensity data is azimuthally integrated over a fine grid. The peak positions and the integrated intensity are calculated for all peaks of interest. The respective integrated intensity values are numerically calculated using the Simpson rule. Peak positions were determined using a similar numerical procedure for the calculation of the centre of mass of the peak. An arbitrary threshold was set to exclude any remaining noise or extremely weak peaks that would not produce reliable results. For the remaining intensities, the centre of mass and the full width at half maximum of each peak was calculated.

The rest of the process can be effectively simplified to peak tracking, with the position of the peak being registered in a 2θ reference for each frame. Finally, the lattice strain ε_i^{hkl} for a given frame i and a given family of lattice planes hkl is calculated as:

$$\varepsilon_i^{hkl} = \frac{d_i^{hkl} - d_0^{hkl}}{d_0^{hkl}} = \frac{\sin\left(\theta_0^{hkl}\right)}{\sin\left(\theta_i^{hkl}\right)} - 1. \tag{2}$$

Data from top and bottom detector panels, as indicated in Fig. 4, are processed and averaged to produce the final lattice strain values with the exception of the 45° dwell experiment where the top panel did not properly trigger, so lattice strains from only the bottom panel were used.

To determine the most appropriate size of the azimuth bin to be considered in the analysis, the data was processed using 10°, 15°, 20° and 30° bins along the loading axis. Due to the texture in the UD plate, bin sizes of less than 10° were avoided as the reduction in the number of grains taken into account both increased the noise and reduced the statistical accuracy of the results. Bin sizes of 15°, 20°, and 30° resulted in comparatively less noise. However, for the case of $\{0002\}$ and $\{11\bar{2}0\}$, the 20° and 30° bins were found to result in overly smooth changes in lattice strain at the beginning of the experiment and as such, the 15° bin was chosen.

An energy (wavelength) correction was also applied to the data to account for small fluctuations in the beam energy. Incoming beam energy was monitored throughout the experiment by intermittent measurements of absorption through a Yb foil. Even though this correction was applied to reduce noise, it made little difference to the processed data with the average offset being 2.05×10^{-5} across all experiments.

A procedure was also developed to estimate uncertainty in the lattice strain measurements. A primary uncertainty (e) related to the signal-to-noise ratio for each peak was calculated using the first 10 frames captured before the specimens were loaded. In the absence of any load, the measured deviation from zero strain was more pronounced for some orientations and planes but in all cases reflected the primary source of uncertainty. This uncertainty is calculated as:

$$e = \frac{1}{n}\sum_{i=1}^{n}|\varepsilon_i| \tag{3}$$

where $n = 10$ is the total number of idle frames. For improved clarity regarding the strain evolution trends with increased cycling, the average value per cycle peak for each *hkl* is calculated.

2.4. Applied Macroscopic Stress

The observed variation of the cross-sectional area, as shown in Fig. 3, necessitated a review of the induced macroscopic stresses to aid interpretation of the various experiments, as well as to confirm that no specimen was loaded too close to the macroscopic yield stress. To this end, the specimens were sectioned at their nominal gauge section and lightly polished to deburr and reveal the sharp cross-sectional outline. The cross-sections were scanned in 2D using an Alicona InfiniteFocus profilometer fitted with a 10x lens.

Each section was scanned twice with a polygon manually fitted around its outline and used to compare each specimen's average cross-sectional area relative to the nominal value. In addition, the applied load of 600 N was divided by the measured area and compared to the orientation-dependent yield stresses σ_y.

These yield strengths were determined through separate small scale tensile tests performed after the X-ray measurements using a Deben 5 kN stage from the same batch of material. For these, the crosshead displacement rate was set to $1\,\mathrm{mm\,min^{-1}}$, which corresponded to an average strain rate of $1.28\times10^{-2}\,\mathrm{s^{-1}}$ in the elastic regime and $1.89\times10^{-1}\,s^{-1}$ in the plastic regime. The 0.2% proof stresses were estimated to be 932 MPa for RD, 904 MPa for 45° and 990 MPa for TD.

It is worth noting that the scans were taken after the experiments and hence the cross-sectional area is that of the deformed state. However, due to the loading being limited to within the macroscopic elastic regime and the relatively small to near-zero accumulation of strain, it is reasonable to assume a negligible change in cross-sectional area. The area data, yield strengths, true applied stress and ratio of applied stress to yield strengths are summarised in Table 3.

Table 3: Overview of estimated macroscopic stresses. The area has been measured after the experiments and σ_y is the orientation-dependent yield stress determined by separate small scale tests. σ is the actual macroscopic stress determined from the true cross-sectional area.

Specimen	**Area (mm^2)**	$\boldsymbol{\sigma_y}$ **(MPa)**	$\boldsymbol{\sigma}$ **(MPa)**	$\boldsymbol{\sigma/\sigma_y}$
RD/Non-Dwell	0.8429	932.4	711.9	0.764
RD/Dwell	0.9545	932.4	628.6	0.674
45°/Non-Dwell	0.8478	903.8	707.7	0.783
45°/Dwell	0.9274	903.8	646.9	0.716
TD/Non-Dwell	0.7850	989.8	764.3	0.772
TD/Dwell	0.7805	989.8	768.7	0.776

Table 3 reveals that the average actual loading is estimated to be 74.8% (standard deviation = 3.9%) of the orientation-specific yield, which despite the deviation from the original target of 85% remains satisfactory for a low-cycle dwell experiment. For Ti64, it has been shown that peak stresses that exceed 85% of the yield accumulate significantly more plastic strain due to cold creep, whereas reduced plastic strain accumulation is observed for values in the 60-80% range [34]. Taking into account the particularly tight tolerances for manufacturing and sectioning, an accumulation of error is to be expected. Crucially, however, it is important to note that all specimens were loaded to a sufficiently sub-yield stress such that the variance should have a negligible effect on the onset of plastic deformation.

2.5. Estimation of Orientation-Dependent Stresses

To further analyse load redistribution among the sets of planes that diffract along the loading axis, it is helpful to estimate the average stresses along that direction from lattice strain measurements using directional moduli. Hooke's law provides the relationship between stress σ_{hkl}, elastic lattice strain ε_{hkl} and elastic moduli E_{hkl} as:

$$\sigma_{hkl} = E_{hkl}\varepsilon_{hkl}. \tag{4}$$

The elastic constants used in the calculation of the directional moduli are taken from Wielewski et al [28] and are (in Voigt notation) $C_{11} = 169$ GPa, $C_{13} = 62$ GPa, $C_{12} = 89.0$ GPa, $C_{44} = 43$ GPa, $C_{33} = 196$ GPa. The calculated directional moduli are summarised in Table 4.

Table 4: Directional moduli for the sets of grains contributing to the diffraction peaks considered.

hkl	$\{10\bar{1}0\}$	$\{0002\}$	$\{01\bar{1}1\}$	$\{01\bar{1}2\}$	$\{11\bar{2}0\}$
Modulus (GPa)	104.4	143.3	109.0	118.5	104.4

3. Results

3.1. Macroscopic Strain Accumulation

The macroscopic strain evolution obtained via DIC is useful for assessing whether the addition of dwell had the expected effect on strain accumulation. Fig. 5 (a) shows the accumulation of macroscopic strain $\Delta\varepsilon_{\text{macroscopic}}$ for specimens loaded under normal cyclic loading conditions, while Fig. 5 (b) shows the accumulation of macroscopic strain in specimens that were cycled with a dwell period at peak load. It is noted that the lighting conditions at the X-ray station were not ideal for DIC measurements leading to an inability to reconstruct macroscopic strain at all points through the non-dwell cyclic loading. Nonetheless, from the instances captured, it can be established that there is no notable accumulation of strain in the absence of dwell periods in any of the specimens.

In the macroscopic strain data for the specimens that were cycled with dwell periods seen in Fig. 5 (b), the 45° specimen stands out as having accumulated a relatively significant amount of strain, reaching up to 4.6×10^{-3}. For both RD and TD specimens, the rate of strain accumulation quickly drops in the first five cycles and becomes fairly stable from the twentieth cycle onwards, ultimately not exceeding 1.0×10^{-3} by the hundredth cycle.

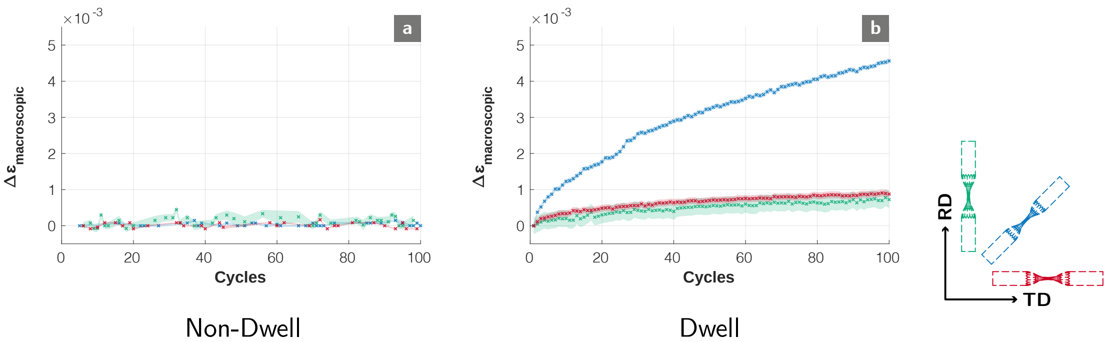

Figure 5: Evolution of peak macroscopic strain (DIC) over 100 cycles for specimens along all tested orientations. (a) shows all specimens subjected to normal (non-dwell) cyclic loading not accumulating any strain. (b) shows the evolution for specimens subjected to a 120 s dwell in each cycle, revealing notable accumulation for the 45° specimen.

3.2. Lattice Strain Evolution

The lattice strain measurements at peak load during each cycle were averaged for all respective families of lattice planes to explore the changes in load distribution with the increasing cycle count. To emphasise the changes in these lattice strains at peak, we define a change of strain $\Delta\varepsilon^{hkl}$ from a given cycle i relative to the first cycle by:

$$\Delta\varepsilon^{hkl} = \varepsilon_i^{hkl} - \varepsilon_0^{hkl}, \tag{5}$$

where ε_0^{hkl} is the respective mean value of the first cycle peak. The calculated lattice strain evolution for all families of α lattice planes from all specimens is shown in Fig. 6. It should be noted that intensities from two families of lattice planes from the β phase were present in the diffraction angle range analysed. However, uncertainties in the positions of these peaks were high due to low intensity and the proximity to α peaks, and as such, they are not presented. For all other measurements, the shaded areas represent the uncertainty as defined in Equation 3. A persistent, elevated uncertainty was identified for the $\{01\bar{1}1\}$ family, predominantly in the specimens along the RD and TD, as the texture and relative orientations led to low intensities along the loading axis.

3.2.1. Non-Dwell Experiments

Initially, the response in the absence of dwell appears fairly consistent between orientations and slip planes, as shown in Fig. 6 (a)-(e) with few and subtle differences noted. Along the RD and TD, cyclic hardening of the planes diffracting along the loading direction has been observed with magnitudes ranging from $-2\times10^{-4} \leq \Delta\varepsilon \leq -4\times10^{-5}$ for all families except $\{01\bar{1}2\}$ where the RD response revealed a larger drop in strain to a magnitude of $\Delta\varepsilon \approx -3.3 \times 10^{-4}$. The basal and prismatic response of the RD and TD specimens consists of a relatively small but sharp drop in strain between the first and second cycle peaks, showing little evolution for the remainder of the experiment. It is also worth noting that despite the sharp initial drop of $\{11\bar{2}0\}$ strain along the RD, it then increases gradually for the remaining cycles (Fig. 6 (e)). Some subtle differences in the elastic response of the 45° experiment are noted; only the $\{01\bar{1}2\}$ system exhibits a clear decrease in lattice strain with applied cycles, measuring a $\Delta\varepsilon \approx -2.2 \times 10^{-4}$ at the end of the experiment. In the 45° experiment, both $\{0002\}$ and $\{01\bar{1}1\}$ lattice strains show a minimal deviation from zero not exceeding $\pm1.0 \times 10^{-4}$ at any point during the experiment. The prismatic response reveals a slight increase which reached a magnitude of up to 1.0×10^{-4} (Fig. 6 (a)).

In the non-dwell specimens, it has been highlighted that some lattice strains show a sharp drop between the first and second cycles. This is most likely attributed to redistribution of residual stresses, which stem primarily from the manufacturing process, but can also be affected by the local texture [35]. This is more pronounced for the RD results and, despite this not being reflected on the macroscopic response, it is relatively significant for systems such as $\{0002\}$ and $\{01\bar{1}0\}$ for which the evolution between first and third cycle is larger than between the third and hundredth cycle.

3.2.2. Dwell Experiments

More pronounced lattice strain evolution is displayed with the addition of dwell, as shown in Fig. 6 (f-j). As anticipated, the TD specimen appears to be the least affected by the hold, as a cyclic drop is also observed for $\{01\bar{1}0\}$, $\{01\bar{1}1\}$ and $\{01\bar{1}2\}$ strains, whereas no notable evolution has been observed for the $\{11\bar{2}0\}$ family. For

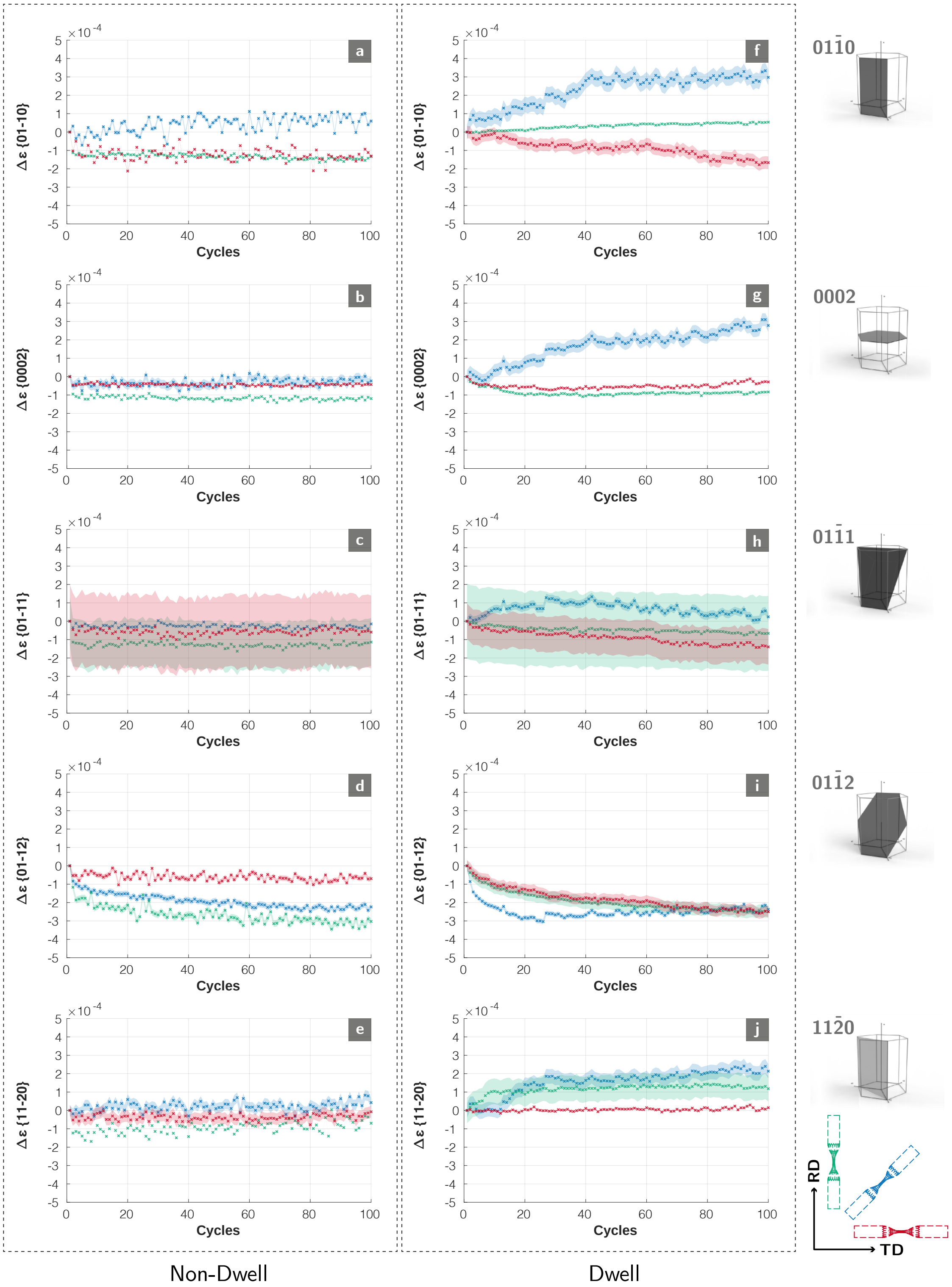

Figure 6: Overview of the lattice strain evolution for the $\{01\bar{1}0\}$ family for non-dwell (a) and dwell (f) loading, for the $\{0002\}$ family for non-dwell (b) and dwell (g) loading, for the $\{01\bar{1}1\}$ family for non-dwell (c) and dwell (h) loading, for the $\{01\bar{1}2\}$ family for non-dwell (d) and dwell (i) loading, for the $\{11\bar{2}0\}$ family for non-dwell (e) and dwell (j) loading.

this orientation, the basal response should be noted as it shows a gradual drop in $\{0002\}$ strain over the first ~ 10 cycles, remaining mostly unchanged over the next ~ 60 cycles and finally showing a small increase in measured lattice strain as the completion of 100 cycles approached.

The RD specimen reveals strong similarities with TD for basal and pyramidal strains, but with key differences in the prismatic families. Even though the magnitude of strain accumulation in $\{01\bar{1}0\}$ is small ($\Delta\epsilon < 6 \times 10^{-5}$), it does represent a switch to cyclic increase when compared to the non-dwell experiment along the same orientation. The $\{11\bar{2}0\}$ strain for the same specimen is much more scattered but exhibits a small increase in the first ~ 8 cycles before plateauing at a magnitude of $\Delta\epsilon < 1.5 \times 10^{-4}$.

The 45° specimen under dwell conditions reveals the largest strain increase between dwell experiments with the most prominent ones exhibiting, on average, a $\Delta\varepsilon \approx 3.1 \times 10^{-4}$ for $\{01\bar{1}0\}$ and $\Delta\varepsilon \approx 3.0 \times 10^{-4}$ for $\{0002\}$ at the end of the experiment. A closer inspection reveals that in most cases the trends change within or at ~ 40 cycles; within the first 10 cycles basal strain slightly fluctuates and drops before stabilising to a positive gradient for the remainder of the dwell experiment. The strain evolution for $\{01\bar{1}1\}$ shows a multitude of gradient changes as it increases more sharply in the first 10 cycles, plateaus irregularly for the following ~ 45 cycles and then begins gently dropping for the remainder of the experiment. Similarly for the $\{01\bar{1}2\}$ family of lattice planes, the 45° specimen records the largest drop in the first 25 cycles which amounts to a $\Delta\varepsilon \approx -3.0 \times 10^{-4}$; from which point the gradient becomes slightly positive. Finally, the second-order prismatic lattice strain reveals a moderate overall increase of $\Delta\varepsilon \approx 2 \times 10^{-4}$ but a decrease is observed over the first ~ 10 cycles followed by an increase over the subsequent ~ 15 cycles before plateauing.

3.3. Orientation-Dependent Stresses

To further characterise load redistribution during the cyclic loading experiments, changes in stress were calculated from the changes in lattice strains presented above. The estimated orientation-dependent stresses for all experiments are shown in Fig. 7. The relative change in lattice strain is multiplied by the previously calculated directional moduli resulting in a $\Delta\sigma$ that is relative to the first cycle peak. Complimentary uncertainties are those calculated for lattice strains, also scaled by the directional moduli. We emphasise here that these stresses assume a uniaxial stress state in all the grains which is well known to not be true. However, these changes in stress do provide some new insights into load redistribution among sets of grains in the volume probed.

Even though the key trends in lattice strain evolution are also reflected in the $\Delta\sigma$ plots, the scaling effect of the respective moduli aids in the identification of further differences between the orientations and the cyclic loading with and without a dwell step.

It is apparent that the addition of dwell periods has a different effect on the evolution of stresses within the RD and TD specimens which macroscopically exhibited

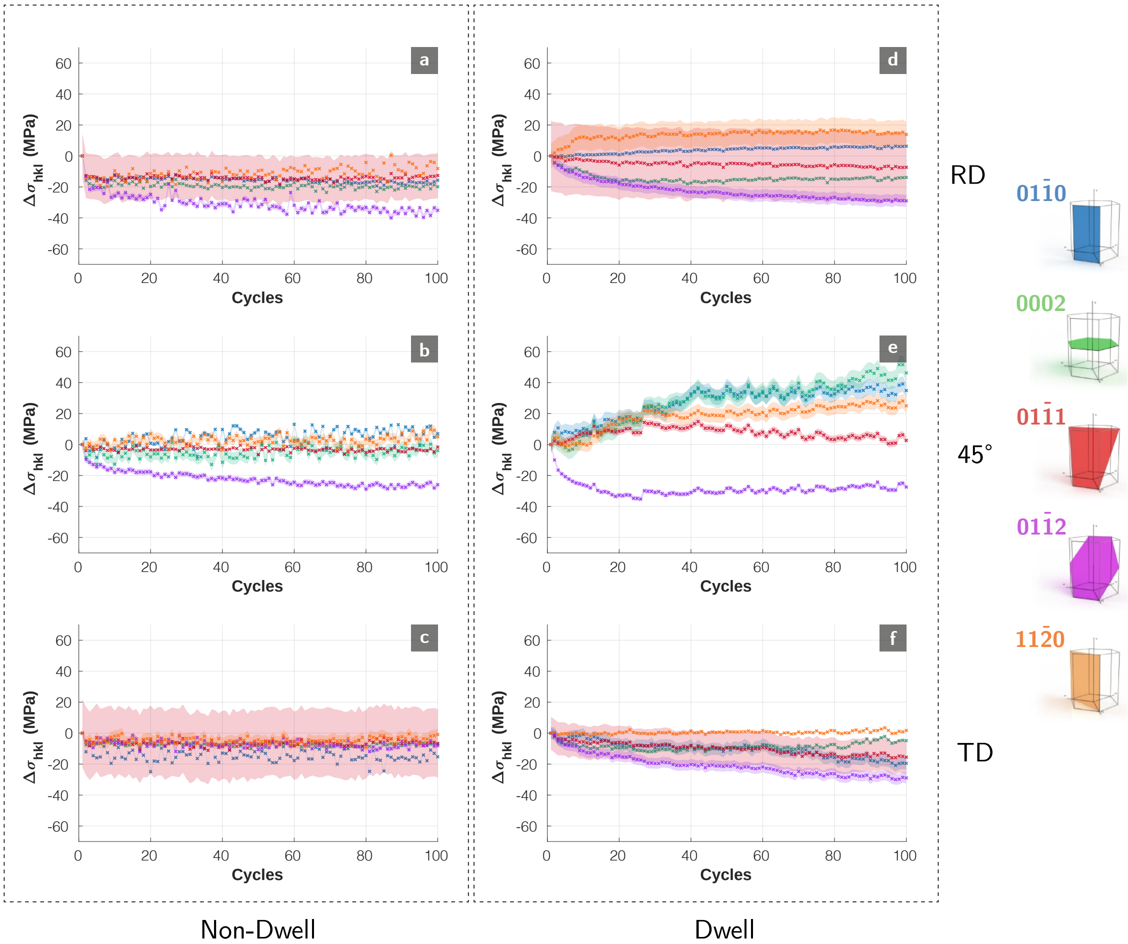

Figure 7: Overview of the calculated stress evolution based on lattice strains for the RD specimens subjected to non-dwell (a) and dwell (d) loading, for the 45° specimens subjected to non-dwell (b) and dwell (e) loading, for the TD specimens subjected to non-dwell (c) and dwell (f) loading.

a very similar and limited dwell debit after 100 cycles. In the most dwell-insensitive orientation, TD, the $\{01\bar{1}0\}$, $\{01\bar{1}1\}$ and $\{01\bar{1}2\}$ stresses closely evolve along a negative trajectory, but $\{0002\}$ stress reflect a flip from a negative to a positive gradient after approximately 70 cycles (Fig. 7 (f)).

The crystallographic conditions present in the 45° non-dwell specimen have led to a different stress evolution under dwell loading. However, it can be seen that the sets of grains contributing to $\{0002\}$ and $\{01\bar{1}0\}$ peaks, with their c axes at 0° and 90° from the loading axis respectively, experience the largest increase in stress which momentarily exceeds 51.5 MPa (Fig. 7 (e)). The 45° specimen subjected to dwell reveals a number of changes in evolution in the first $\sim$ 25 cycles, but thereafter, there is a divergence between $\{01\bar{1}0\}$, $\{0002\}$ and $\{11\bar{2}0\}$ which keep increasing and $\{01\bar{1}1\}$ which keeps decreasing.

4. Discussion

The macroscopic and lattice strain response of UD-rolled Ti64 has been captured in-situ under cyclic (non-dwell) and 120 s dwell conditions over 100 cycles. The form of the alloy chosen presents a crystallographically intriguing case, which allowed MTRs to be subjected to loading at different orientations relative to the dominant macrozone orientation by extracting specimens along the plate's RD, TD and 45° between the two. These measurements reveal subtle but key differences arising from the combination of dwell and orientations effects related to the MTRs. This study complements a wide range of research on titanium alloys for aerospace applications [8] and relatively recent incidents of in-service components being heavily affected by the material's texture [36] highlight the need for continuous and in-depth reviews of our understanding of key deformation mechanisms.

4.1. Macroscopic Response

Macroscopic strain measurements obtained via DIC reveal no appreciable accumulation of strain in any of the tested orientations over the course of the non-dwell experiments. When subjected to dwell, the macroscopic response changes to reveal limited evolution for both RD and TD specimens, which did not exceed 1.0×10^{-3}, but a significant accumulation of 4.6×10^{-3} was recorded for the 45° specimen. The rate of strain accumulation in the 45° specimen declines quickly in the first 40 cycles but starts stabilising onwards to an average rate of 2.78×10^{-5} per cycle.

To further aid in the interpretation of this result prior to considering the grain-scale response, EBSD data has been used to calculate the maximum basal and prismatic Schmid factor (SF) across the cross-sections of the dwell specimens, which are shown in Fig. 8. Even though the maps represent only a slice of the sampled volume for diffraction, they offer a representative view of the sites likely to experience the highest resolved shear stresses during loading. As shown in Fig. 2, the rolling process causes many grains to preferentially align their c axis with the TD and, as such, it is sensible that the 45° specimen presents the most favourable case for basal slip. In addition, Fig. 8(b) reveals a high basal SF distribution over almost the entirety of the cross-section, suggesting a synergy of grains that are part of TD-oriented macrozones and some grains in the weaker-textured regions with equally high SFs (primarily those that are oriented along the RD). The same specimen shows a moderate distribution of prismatic SFs in Fig. 8(e), suggesting that prismatic slip could also be activated particularly after grains favourable for basal slip have been significantly deformed and lost their load-carrying capability. The second-highest average SF has been observed for the prismatic family in the RD specimen (Fig. 8(d)), which did not manifest itself in a significant accumulation of macroscopic strain. The TD specimen also shows a moderate basal SF distribution (Fig. 8(c)), which is largely counteracted by the macrozones displaying extremely low prismatic SFs (Fig. 8(f)).

4.2. Grain-scale Response

The peak lattice strain in cyclic (non-dwell) fatigue showed little evolution that didn't exceed $|\Delta\varepsilon| \leq 1.5 \times 10^{-4}$ over 100 cycles for all specimens, with the exception

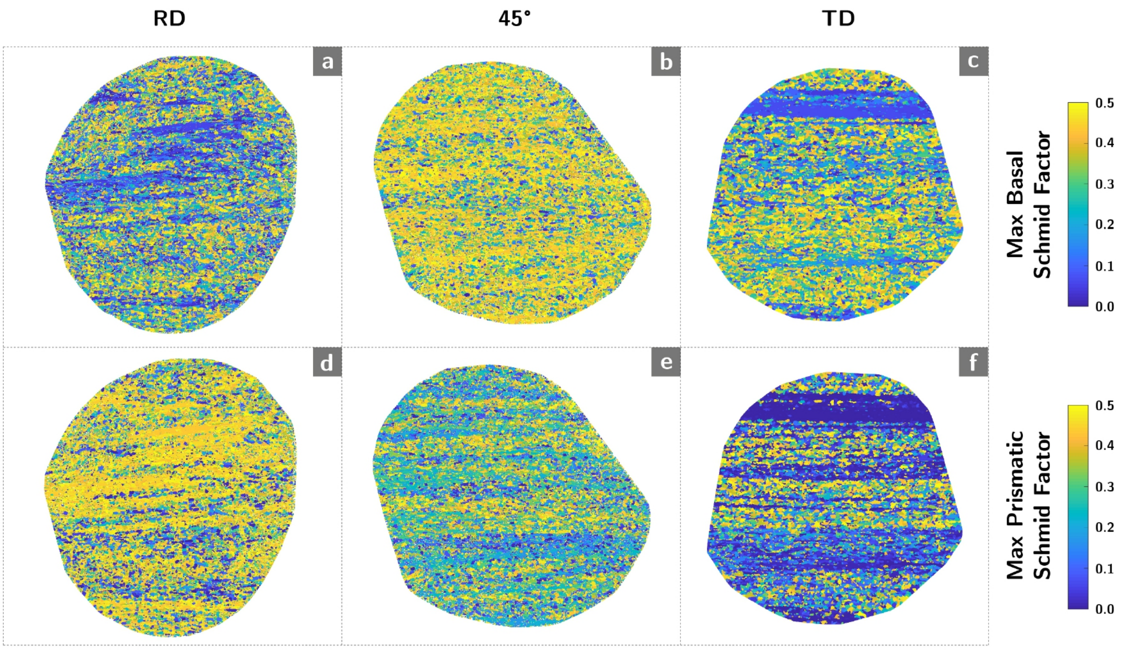

Figure 8: Overview of the calculated Schmid factors based on the EBSD data for the basal family and the RD (a), 45° (b) and TD (c) specimens, as well as the prismatic family and the RD (d), 45° (e) and TD (f) specimens.

of the $\{01\bar{1}2\}$ family which recorded a drop of up to $\Delta\varepsilon \approx -3.4 \times 10^{-4}$ in the RD specimen. This apparent cyclic hardening behaviour might seem consistent at first since it concerns a family with a high critical resolved shear stress relative to basal or prismatic, but at this point, it is important to make a distinction between easy/hard planes to slip and where each of these measurements come from. For example, it is known that a grain with its c axis 45° away from the loading axis, experiences higher basal stress than in any other orientation, but such a grain would also diffract an incoming beam 45° away from the loading axis on the diffraction ring. The measurements displayed in Fig. 6 stem from diffracted points within 7.5° of the loading axis. This is consistent with the azimuth bin chosen for the analysis, as the 15° segment symmetrically stretches over both sides of the loading axis corresponding to a deviation of up to 7.5° in any direction. As such, a 'soft' grain for basal slip does not contribute its basal lattice strain response along the loading axis, but 45° away from it. However, in the same grain, the $\{01\bar{1}2\}$ plane is approximately 42.4° away from the basal plane and that would, in fact, diffract within 7.5° of the loading axis.

It is worth noting that the mechanical response from a region of the material wholly taken up by a macrozone is significantly different from a weak-textured region, as the former behaves more like a single grain. In production materials, both of these distinct regions exist, but the inherent differences in mechanical properties lead to strain localisation [37, 38]. Regarding the interpretation of the diffraction data, this means that virtually all grains with an orientation along the dominant macrozone orientation (TD) will only contribute measurements to one family, whereas the rest

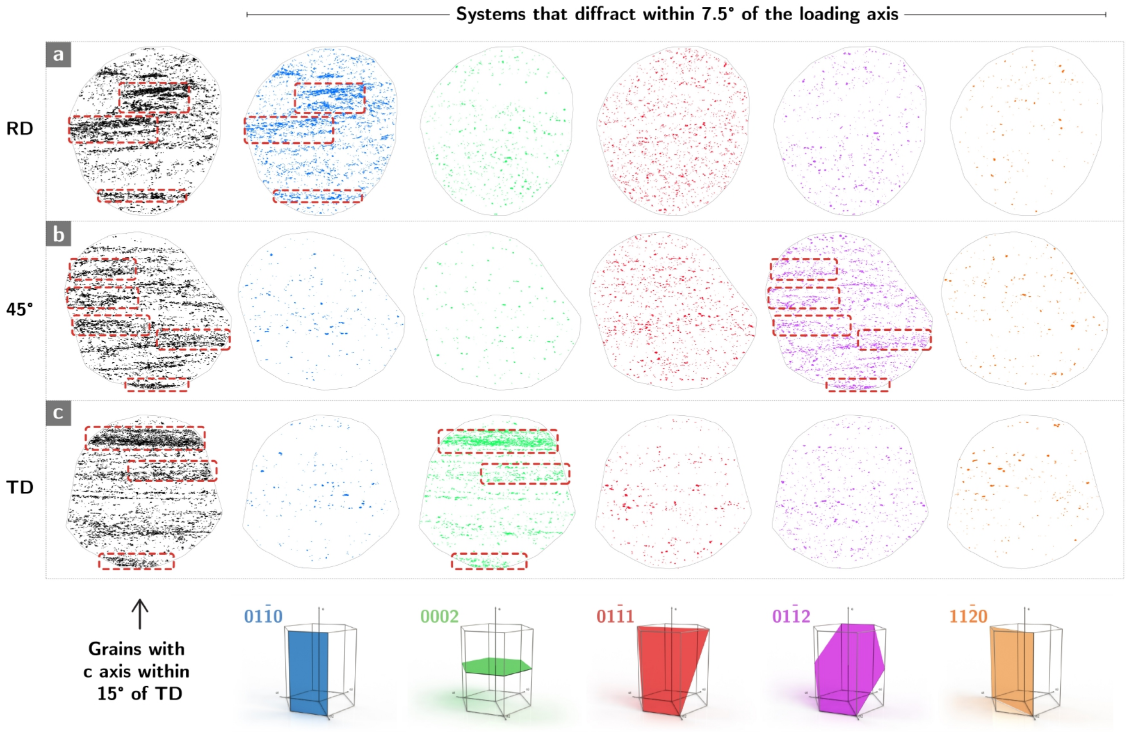

Figure 9: Fibres of orientations calculated from the EBSD data, highlighting which grains have c axes within 15° of the dominant macrozone orientation, TD. On their right, EBSD data for all grains is used to highlight the respective crystal planes that would diffract the incident beam within 7.5° of the loading axis for the RD (a), 45° (b) and TD (c) specimens. The dotted red boxes highlight some of the more prominent MTRs and the corresponding families they diffract from.

will be measured only from the weaker-textured regions. More crucially, the family that macrozones contribute lattice measurements to is different in all three cases examined. To further clarify this, the EBSD data has been used to visualise orientation fibres contributing to diffraction along the loading axis are shown in Fig. 9. On the left of the figure, a threshold map highlights grains with c axes along the TD, while the plots on the right highlight all respective α planes with normal plane vectors pointing within 7.5° of the loading axis.

Even though Fig. 9(b) confirms that grains within the 45° specimen's macrozones predominantly contribute to the $\{01\bar{1}2\}$ measurement along the loading axis, closer inspection in conjunction with Fig. 8(a) and (c) reveals that high basal SF areas are primarily represented by $\{01\bar{1}2\}$ measurements for the RD and TD specimens too. In essence, the drop in $\{01\bar{1}2\}$ family strain for both RD and 45° specimens is most likely a reflection of basal slip taking place in those grains. The stress redistribution causes an ever-reducing load to be applied to those grains and, subsequently, being resolved onto $\{01\bar{1}2\}$. Even in the absence of dwell, the role of the β phase in early deformation should not be discounted [39–41] but this could not be examined in this case for either $\{110\}$ or $\{020\}$.

The addition of the dwell period had an observable effect on all specimens at the lattice level. The RD specimen, despite having high prismatic SFs (Fig. 8(d)) and with those same grains contributing to the measured prismatic response (Fig. 9(a)) only recorded a marginal increase in $\{01\bar{1}0\}$ family strain. High stresses in macrozones with predominantly prismatic orientations have been shown to interact with basal textures that eventually lead to cracks forming at their interface [42]. In this case, the prismatic macrozones did not manage to sufficiently interact with favourable basal planes, possibly due to the absence of enough favourably oriented neighbours. Even though the TD specimen subjected to dwell loading shows a drop in $\{01\bar{1}0\}$, $\{01\bar{1}1\}$ and $\{01\bar{1}2\}$ family strain, the overall behaviour is dominated by macrozones which are oriented unfavourably for both basal and prismatic slip. Those macrozones only directly contribute measurements to the $\{0002\}$ family, which shows little evolution in support of the previous statement. From both Fig. 8(f) and Fig. 9(c), it can be suggested that the prismatic response for the TD specimen which showed a gradual drop over the course of the experiment stems from relatively fewer grains in the weak-textured region which also has high prismatic SF and indicates that some prismatic slip may have taken place but at a very limited scale and fully surrounded by much stronger-textured regions.

In the particular case of the 45° specimen, the anticipated response is captured macroscopically, but as Fig. 9(b) confirms, both the $\{01\bar{1}0\}$ and $\{0002\}$ family responses stem from grains in the weak-textured regions. Even though the lattice strain response might seem slightly more erratic in the first $\sim$ 25 cycles it could not be attributed to an external factor (such as loss of grip), as no strong discontinuities are present in the macroscopic strain (DIC) data. As such, the observed response most likely reflects the complex stress redistribution taking place during the early deformation cycles. As noted, the macrozones in this specimen have only contributed to the $\{01\bar{1}2\}$ response.

However, if one takes into account the relative orientation relationships discussed so far and consults Figs. 6(f), (g), and (i) in tandem, a chain of events can be postulated. In this specimen, the $\{01\bar{1}2\}$ family exhibits the fastest strain drop in 25 cycles among all families and all experiments while also being an indirect reflection of the conditions within the macrozones (Fig. 9(b)) and some of the other areas with very high basal SF (Fig. 8(b)). While this is taking place, both the $\{01\bar{1}0\}$ and $\{0002\}$ family strains increase, at a slightly faster rate for the prismatic family which plateaus after the fortieth cycle, while the basal strain keeps increasing over the course of the experiment. Even though both $\{01\bar{1}0\}$ and $\{0002\}$ measurements come from weak-textured regions, only the former displays very high SFs which could elucidate why the $\{01\bar{1}0\}$ response plateaus after a point. Overall, this would suggest widespread basal slip in the MTRs from the first few dwell applications which significantly slows down after approximately thirty cycles, as indicated by the $\{01\bar{1}2\}$ response. As this is taking place, some of the initial load is being redistributed to grains with their c axes at $0°\pm7.5°$ to the loading axis (suggested through the $\{0002\}$ response) and grains with their c axes at $90°\pm7.5°$ (suggested through the $\{01\bar{1}0\}$ response), with one important distinction being that after the fortieth cycle some wider prismatic slip is also taking place outside the MTRs. This is in line with findings from recently published work [43] which showed that in cases where basal slip is active but the load is not sufficiently high to initially activate slip on other planes, the cyclic redistribution of load leads to concurrent slip with the number of active slip systems increasing as the accumulated plastic strain also increased. The {0002} family keeps accumulating elastic strain over the course of the experiment and ultimately such grains (with c axis $0°\pm7.5°$ away from the loading axis) become prime candidates for facet formation sites [3]. Even though the dwell mechanism is associated with a plastic strain debit which cannot be captured in these measurements, the indirect shifts in lattice strain gradients that it caused are instrumental in interpreting the mechanism's progression.

The utilisation of the captured data along with the approximation of the directional moduli enabled the estimation of the stresses the lattice experienced and highlighted further differences. The 45° specimen exhibits the most rapid change in stress, of $\Delta\sigma \approx -32.7\,\text{MPa}$ for $\{01\bar{1}2\}$ within the first twenty cycles and the largest increase of $\Delta\sigma \approx 51.5\,\text{MPa}$ for the {0002} family towards the end of the experiment. The effects of stress redistribution due to residual stresses were more pronounced for some of the non-dwell experiments as the largest change in stress has been observed in the first few cycles. The stress evolution plots also highlight that stresses in the TD specimen subjected to dwell either remained unchanged ($\{11\bar{2}0\}$) or decreased over the course of the experiment. The necessity for balance in stress redistribution, particularly in a specimen with very limited macroscopic evolution, suggests that stress must have increased in either the β phase or in groups of α families that did not diffract near the loading axis or were affected by texture inhomogeneity.

4.3. Size Effects

The occurrence of more or less favourable orientations for slip in macrozones presents further challenges, as their nature is such that they do not pose significant barriers to slip transmission within the MTR itself. Even though some work has been done to examine the progression of deformation mechanisms at the interface of macrozones and weak-textured regions [16, 17, 19], an important consideration, in this case, is that some of the macrozones are not fully or sufficiently enclosed by a weak-textured matrix. A computational study by Liu and Dunne [44] noted that high-aspect macrozones that are fully subsurface are more damaging than those that intersect free surfaces. However, this has not been validated experimentally and based on these experiments, cases where one or more macrozones are found to intersect free surfaces on one or both ends should not be necessarily discounted as less sensitive to dwell fatigue. For this case, the potential for an augmented influence of the MTRs due to their relative volume to the sample volume at gauge has been considered and will be the topic of subsequent investigation.

Even though rectangular specimens are known to underperform compared to round ones for some materials, both in tensile tests [45] and under fatigue [46], the choice of the hexadecagon as a feasible cross-section and the manufacturing limitations imposed a sizing error that was difficult to quantify in-situ. Efforts were subsequently made to quantify the variation and this was found to be moderate while confirming that no specimen was overloaded with the average actual stress being determined to be $\sim 74.8\%$ of the orientation-dependent yield stress for UD-rolled Ti64. We note that although there was variation in loading conditions, the dwell specimens all exhibited the most prominent load redistribution with cyclic loading, even though these specimens tended to have lower peak stresses. A peak stress of 60% of the yield is often cited as the lowest necessary for the onset of dwell due to Ti64 undergoing cold creep at these stress levels [47], although this has not been rigorously validated in a cold-dwell fatigue context. Other studies have indicated that dwell effects are considered to become prominent at stresses that are approximately $\geqslant 75\%$ of the yield stress [2]. In this study, despite the deviation from the target stress level of 85%, all specimens were cycled above 60% of the yield stress and all but two were cycled above 75% of the yield stress. The 45° specimen subjected to dwell was one of the two cycled below the 75% yield stress threshold, but showed comparatively large plastic strain accumulation over 100 cycles. This represents a useful result as it captures the dwell evolution at a stress that minimises the risk of other mechanisms, such as plastic ratcheting, playing a significant role in the deformation. The RD specimen subjected to dwell was the only specimen loaded to less than 70% of the yield stress and this loading places it close to the roughly defined threshold of dwell-sensitive stresses. However, the subtle evolution of the lattice response indicates that a certain amount of load redistribution had taken place even in this specimen. These results suggest that dwell fatigue may be operative at relatively low stress levels and should be the subject of further investigation. For future work, it is worth reconsidering the choice of simpler cross-sections or other manufacturing methods. Furthermore, smaller specimens have been known to underperform in dwell fatigue testing; experiments by Song and Hoeppner on IMI 829 support this argument [48], but the ability to probe the entire gauge volume justified the choice of size.

5. Conclusions

The role of large microtextured regions in Ti64 and dwell fatigue has been examined using high energy X-ray diffraction with the dominant MTR orientation aligned with the loading axis, perpendicular to the loading axis and at 45°. Specimens were subjected to cyclic (non-dwell) and 120 s dwell loading for 100 cycles at an average of 74.8% of the orientation-dependent yield stress.

- In the absence of dwell, the rolled material exhibits near zero or subtly declining strains at the grain level over 100 cycles with the dominant macrozone orientation c axis both aligned with the loading axis (TD) and with it lying perpendicular to the loading axis (RD).
- Despite not showing signs of significant dwell debit macroscopically, both the RD and TD specimens display a different evolution of peak lattice strains under the application of the dwell hold when compared to the respective non-dwell responses.
- A complex redistribution of stresses at the grain level has been captured within the first 25 cycles of dwell fatigue for the 45° specimen. The uniformly high maximum basal SF distribution across the specimen's cross-section contributed to notable macroscopic strain accumulation which increased by 4.6×10^{-3} over the course of the experiment.

- The 45° specimen recorded the quickest drop in $\{01\bar{1}2\}$ family strain, reaching -3.0×10^{-4} in 25 cycles. An examination of the diffraction fibres and the crystallographic conditions of the grains contributing to each family's response indicated that this response stems from grains within the MTR with high basal SFs. In the first 40 cycles, the largest increase in lattice strain has been observed for the $\{01\bar{1}0\}$ and $\{0002\}$ families, which postulated that at least a proportion of the load being redistributed following the early basal slip is being received by grains in the weak-textured matrix with their c axes at 90°±7.5° and 0°±7.5° away from the loading axis respectively.

Acknowledgements

This research was carried out with the technical and financial support of Rolls-Royce plc and the EPSRC NPIF under award 1953429. This work is based upon research conducted at the Cornell High Energy Synchrotron Source (CHESS) under NSF award DMR-1332208 and the Center for High Energy X-ray Science (CHEXS) which is supported by NSF award DMR-1829070. The authors would like to thank Prof David Rugg, Dr Mark Dixon and Dr Euan Wielewski for their invaluable contributions and support.

Conflict of Interest

The authors declare that they have no conflicts of interest.

Data Availability

The raw and processed data required to reproduce these findings cannot be shared at this time as the data also forms part of an ongoing study.

References

[1] G. Lutjering, J. Williams, Titanium, 2nd Edition, Springer, Heidelberg, 2007.

[2] M. Bache, Dwell sensitive fatigue in a near alpha titanium alloy at ambient temperature, International Journal of Fatigue 19 (93) (1997) 83–88. doi:10.1016/S0142-1123(97)00020-0.

[3] W. J. Evans, M. R. Bache, Dwell-sensitive fatigue under biaxial loads in the near-alpha titanium alloy IMI685, International Journal of Fatigue 16 (7) (1994) 443–452. doi:10.1016/0142-1123(94)90194-5.

[4] W. J. Evans, C. R. Gostelow, The effect of hold time on the fatigue properties of a β-processed titanium alloy, Metallurgical Transactions A 10 (12) (1979) 1837–1846. doi:10.1007/BF02811727.

[5] A. Woodfield, M. Gorman, J. Sutliff, R. Corderman, Effect of Microstructure on Dwell Fatigue Behavior of Ti-6242, in: Titanium'95: Science and technology, 1995, pp. 1116–1123.

[6] Z. Zheng, D. S. Balint, F. P. E. Dunne, Discrete dislocation and crystal plasticity analyses of load shedding in polycrystalline titanium alloys, International Journal of Plasticity 87 (2016) 15–31. doi:10.1016/j.ijplas.2016.08.009.

[7] J. Kumar, A. K. Singh, S. G. S. Raman, V. Kumar, Microtexture Analysis and Modeling of Ambient Fatigue and Creep-Fatigue Damages in Ti-6Al-4V Alloy, Metallurgical and Materials Transactions A (2016). doi:10.1007/s11661-016-3869-9.

[8] M. R. Bache, A review of dwell sensitive fatigue in titanium alloys: The role of microstructure, texture and operating conditions, International Journal of Fatigue 25 (9-11) (2003) 1079–1087. doi:10.1016/S0142-1123(03)00145-2.

[9] M. R. Bache, L. Germain, T. Jackson, A. R. M. Walker, Mechanical and texture rvaluations of Ti 6246 as a dwell fatigue tolerant alloy, in: Ti-2007 Science and Technology, The Japan Institute of Metals, 2007, pp. 523–526.

[10] F. P. E. Dunne, D. Rugg, On the mechanisms of fatigue facet nucleation in titanium alloys, Fatigue and Fracture of Engineering Materials and Structures 31 (11) (2008) 949–958. doi:10.1111/j.1460-2695.2008.01284.x.

[11] L. Yang, J. Liu, J. Tan, Z. Chen, Q. Wang, R. Yang, Dwell and normal cyclic fatigue behaviours of Ti60 alloy, Journal of Materials Science and Technology 30 (7) (2014) 706–709. doi:10.1016/j.jmst.2013.10.010.

[12] M. Cuddihy, A. Stapleton, S. Williams, F. Dunne, On cold dwell facet fatigue in titanium alloy aero-engine components, International Journal of Fatigue 97 (2017) 177–189. doi:10.1016/j.ijfatigue.2016.11.034.

[13] E. E. Sackett, L. Germain, M. R. Bache, Crystal plasticity, fatigue crack initiation and fatigue performance of advanced titanium alloys, International Journal of Fatigue 29 (9-11) (2007) 2015–2021. doi:10.1016/j.ijfatigue.2006.12.011.

[14] Z. Zhang, D. E. Eakins, F. P. Dunne, On the formation of adiabatic shear bands in textured HCP polycrystals, International Journal of Plasticity 79 (2016) 196–216. doi:10.1016/j.ijplas.2015.12.004.

[15] I. Bantounas, D. Dye, T. C. Lindley, The role of microtexture on the faceted fracture morphology in Ti-6Al-4V subjected to high-cycle fatigue, Acta Materialia 58 (11) (2010) 3908–3918. doi:10.1016/j.actamat.2010.03.036.

[16] K. Le Biavant, S. Pommier, C. Prioul, Local texture and fatigue crack initiation in a Ti-6Al-4V titanium alloy, Fatigue and Fracture of Engineering Materials and Structures 25 (6) (2002) 527–545. doi:10.1046/j.1460-2695.2002.00480.x.

[17] S. Hémery, V. T. Dang, L. Signor, P. Villechaise, Influence of Microtexture on Early Plastic Slip Activity in Ti-6Al-4V Polycrystals, Metallurgical and Materials Transactions A: Physical Metallurgy and Materials Science 49 (6) (2018) 2048–2056. doi:10.1007/s11661-018-4569-4.

[18] K. Zhang, K. V. Yang, A. Huang, X. Wu, C. H. Davies, Fatigue crack initiation in as forged Ti-6Al-4V bars with macrozones present, International Journal of Fatigue 80 (2015) 288–297. doi:10.1016/j.ijfatigue.2015.05.020.

[19] A. L. Pilchak, A simple model to account for the role of microtexture on fatigue and dwell fatigue lifetimes of titanium alloys, Scripta Materialia 74 (2014) 68–71. doi:10.1016/j.scriptamat.2013.10.024.

[20] M. Bache, W. Evans, Impact of texture on mechanical properties in an advanced titanium alloy, Materials Science and Engineering: A 319-321 (2001) 409–414. doi:10.1016/S0921-5093(00)02034-7.

[21] I. Bantounas, T. C. Lindley, D. Rugg, D. Dye, Effect of microtexture on fatigue cracking in Ti-6Al-4V, Acta Materialia 55 (16) (2007) 5655–5665. doi:10.1016/j.actamat.2007.06.034.

[22] A. M. Stapleton, S. L. Raghunathan, I. Bantounas, H. J. Stone, T. C. Lindley, D. Dye, Evolution of lattice strain in Ti-6Al-4V during tensile loading at room temperature, Acta Materialia 56 (20) (2008) 6186–6196. doi:10.1016/j.actamat.2008.08.030.

[23] J. V. Bernier, J. S. Park, A. L. Pilchak, M. G. Glavicic, M. P. Miller, Measuring stress distributions in Ti-6Al-4V using synchrotron X-ray diffraction, Metallurgical and Materials Transactions A: Physical Metallurgy and Materials Science 39 (13) (2008) 3120–3133. doi:10.1007/s11661-008-9639-6.

[24] L. Wang, Z. Zheng, H. Phukan, P. Kenesei, J. S. Park, J. Lind, R. M. Suter, T. R. Bieler, Direct measurement of critical resolved shear stress of prismatic and basal slip in polycrystalline Ti using high energy X-ray diffraction microscopy, Acta Materialia 132 (2017) 598–610. doi:10.1016/j.actamat.2017.05.015.

[25] Y. Xiong, P. Karamched, C.-T. Nguyen, C. M. Magazzeni, E. Tarleton, A. J. Wilkinson, Cold Creep of Titanium: Analysis of Stress Relaxation Using Synchrotron Diffraction and Crystal Plasticity Simulations, SSRN Electronic Journal (2020). doi:10.2139/ssrn.3558273.

[26] K. Chatterjee, J. Y. Ko, J. T. Weiss, H. T. Philipp, J. Becker, P. Purohit, S. M. Gruner, A. J. Beaudoin, Study of residual stresses in Ti-7Al using theory and experiments, Journal of the Mechanics and Physics of Solids 109 (2017) 95–116. doi:10.1016/j.jmps.2017.08.008.

[27] P. R. Dawson, D. E. Boyce, J.-s. Park, E. Wielewski, M. P. Miller, Determining the strengths of HCP slip systems using harmonic analyses of lattice strain distributions, Acta Materialia 144 (2018) 92–106. doi:10.1016/j.actamat.2017.10.032.

[28] E. Wielewski, D. E. Boyce, J.-S. Park, M. P. Miller, P. R. Dawson, A methodology to determine the elastic moduli of crystals by matching experimental and

simulated lattice strain pole figures using discrete harmonics, Acta Materialia 126 (2017) 469–480. doi:10.1016/j.actamat.2016.12.026.

[29] EDAX, OIM Analysis (Accessed on 11/05/2021) (2021).
URL `https://www.edax.com/products/ebsd/oim-analysis`

[30] F. Bachmann, R. Hielscher, H. Schaeben, Texture Analysis with MTEX – Free and Open Source Software Toolbox, Solid State Phenomena 160 (2010) 63–68. doi:10.4028/www.scientific.net/SSP.160.63.

[31] I. Bantounas, D. Dye, T. C. Lindley, The Effect of Grain Orientation on Fracture Morphology during the High Cycle Fatigue of Ti-6Al-4V, Acta Materialia 57 (12) (2009) 3584–3595. doi:https://doi.org/10.1016/j.actamat.2009.04.018.

[32] GOM GmbH, GOM Correlate - Software for 3D Testing Data (Accessed on 11/05/2021) (2021).
URL `https://www.gom.com`

[33] J. V. Bernier, N. R. Barton, U. Lienert, M. P. Miller, Far-field high-energy diffraction microscopy: A tool for intergranular orientation and strain analysis, Journal of Strain Analysis for Engineering Design 46 (7) (2011) 527–547. doi:10.1177/0309324711405761.

[34] G. Xi, J. Lei, J. Qiu, Y. Ma, R. Yang, A semi-quantitative explanation of the cold dwell effect in titanium alloys, Materials and Design 194 (2020) 108909. doi:10.1016/j.matdes.2020.108909.

[35] J. S. Park, A. K. Ray, P. R. Dawson, U. Lienert, M. P. Miller, Determination of residual stress in a microtextured α titanium component using high-energy synchrotron X-rays, Journal of Strain Analysis for Engineering Design 51 (5) (2016) 358–374. doi:10.1177/0309324716640419.

[36] BEA, Accident to the AIRBUS A380-861 equipped with Engine Alliance GP7270 engines registered F-HPJE operated by Air France on 30 September 2017 in cruise over Greenland (Denmark), Tech. Rep. September, Bureau d'Enquêtes et d'Analyses (2020).

[37] D. Lunt, J. Q. da Fonseca, D. Rugg, M. Preuss, Microscopic strain localisation in Ti-6Al-4V during uniaxial tensile loading, Materials Science and Engineering A 680 (October 2016) (2017) 444–453. doi:10.1016/j.msea.2016.10.099.

[38] J. Cappola, J.-C. Stinville, M.-A. Charpagne, P. G. Callahan, M. P. Echlin, T. M. Pollock, A. Pilchak, M. Kasemer, On the Localization of Plastic Strain in Microtextured Regions of Ti-6Al-4V, Acta Materialia (2020) 116492doi:10.1016/j.actamat.2020.116492.

[39] S. Waheed, Z. Zheng, D. S. Balint, F. P. Dunne, Microstructural effects on strain rate and dwell sensitivity in dual-phase titanium alloys, Acta Materialia 162 (September) (2018) 136–148. doi:10.1016/J.ACTAMAT.2018.09.035.

[40] A. L. Pilchak, G. A. Sargent, S. L. Semiatin, Early Stages of Microstructure and Texture Evolution during Beta Annealing of Ti-6Al-4V, Metallurgical and Materials Transactions A: Physical Metallurgy and Materials Science 49 (3) (2018) 908–919. doi:10.1007/s11661-017-4444-8.

[41] S. Hémery, P. Villechaise, D. Mellier, On the Role of the Beta Phase on Slip Activity in Ti-6Al-4V Single Colonies, in: A. Venkatesh, A. L. Pilchak, J. E. Allison, S. Ankem, R. Boyer, J. Christodoulou, H. L. Fraser, M. A. Imam, Y. Kosaka, H. J. Rack, A. Chatterjee, A. Woodfield (Eds.), Proceedings of the 13th World Conference on Titanium, TMS (The Minerals, Metals & Materials Society), 2016, pp. 1121–1128. doi:10.1002/9781119296126.ch190.

[42] S. Hémery, A. Naït-Ali, M. Guéguen, J. Wendorf, A. T. Polonsky, M. P. Echlin, J. C. Stinville, T. M. Pollock, P. Villechaise, A 3D analysis of the onset of slip activity in relation to the degree of micro-texture in Ti–6Al–4V, Acta Materialia 181 (2019) 36–48. doi:10.1016/j.actamat.2019.09.028.

[43] C. Lavogiez, S. Hémery, P. Villechaise, Analysis of deformation mechanisms operating under fatigue and dwell-fatigue loadings in an α/β titanium alloy, International Journal of Fatigue 131 (July 2019) (2020) 105341. doi:10.1016/j.ijfatigue.2019.105341.
URL `https://doi.org/10.1016/j.ijfatigue.2019.105341`

[44] Y. Liu, F. P. Dunne, The mechanistic link between macrozones and dwell fatigue in titanium alloys, International Journal of Fatigue 142 (October 2020) (2021) 105971. doi:10.1016/j.ijfatigue.2020.105971.

[45] M. Fellner, E. Pink, The Influence of the Cross-section Shape of Specimens on Strength Characteristics Under Conditions of Inhomogeneous Flow, Scripta Metallurgica 27 (8) (1992) 259–264.

[46] N. Kawagoishi, H. Nisitani, X. Wang, H. Ide, H. Tanaka, Effect of Cross-Sectional Shape of Specimen on Fatigue Strength under Plane Bending., Transactions of the Japan Society of Mechanical Engineers Series A 62 (595) (1996) 607–613. doi:10.1299/kikaia.62.607.

[47] B. C. Odegard, A. W. Thompson, Low temperature creep of Ti-6 Al-4 V, Metall Trans 5 (5) (1974) 1207–1213. doi:10.1007/BF02644335.

[48] Z. Song, D. W. Hoeppner, Size effect on the fatigue behaviour of IMI 829 titanium alloy under dwell conditions, International Journal of Fatigue 11 (2) (1989) 85–90. doi:10.1016/0142-1123(89)90002-9.